Springer

Acta Mechanica Sinica

CrossMark click for updates

• RESEARCH PAPER •

Acta Mech. Sin., Vol. 40, 423639 (2024)
https://doi.org/10.1007/s10409-024-23639-x

A novel videogrammetry-based full-field dynamic deformation monitoring method for variable-sweep wings

Liqiang Gao[1,2], Yan Liu[3,4*], Bin Jiang[2], Zhendong Ge[2], Haoyang Li[2], Xiang Guo[2], Tao Suo[2], and Qifeng Yu[1,2,3,4*]

[1] *School of Civil Aviation, Northwestern Polytechnical University, Xi'an 710072, China;*
[2] *Shaanxi Key Laboratory of Impact Dynamics and Engineering Application, Northwestern Polytechnical University, Xi'an 710072, China;*
[3] *College of Physics and Optoelectronic Engineering, Shenzhen University, Shenzhen 518060, China;*
[4] *Institute of Intelligent Optical Measurement and Detection, Shenzhen University, Shenzhen 518060, China*

Received December 17, 2023; accepted March 7, 2024; published online June 11, 2024

The measurement of wing dynamic deformation in morphing aircraft is crucial for achieving closed-loop control and evaluating structural safety. For variable-sweep wings with active large deformation, this paper proposes a novel videogrammetric method for full-field dynamic deformation measurement. A stereo matching method based on epipolar geometry constraint and topological constraint is presented to find the corresponding targets between stereo images. In addition, a new method based on affine transformation combined with adjacent closest point matching is developed, aiming to achieve fast and automatic tracking of targets in time-series images with large deformation. A calculation model for dynamic deformation parameters is established to obtain the displacement, sweep variable angle, and span variation. To verify the proposed method, a dynamic deformation measurement experiment is conducted on a variable-sweep wing model. The results indicate that the actual accuracy of the proposed method is approximately 0.02% of the measured area (e.g., 0.32 mm in a 1.6 m scale). During one morphing course, the sweep variable angle, the span variation and the displacement increase gradually, and then decrease. The maximum sweep variable angle is 36.6°, and the span variation is up to 101.13 mm. The overall configuration of the wing surface is effectively reconstructed under different morphing states.

Morphing aircraft, Variable-sweep wing, Videogrammetry, Large dynamic deformation, Target matching and tracking

Citation: L. Gao, Y. Liu, B. Jiang, Z. Ge, H. Li, X. Guo, T. Suo, and Q. Yu, A novel videogrammetry-based full-field dynamic deformation monitoring method for variable-sweep wings, Acta Mech. Sin. 40, 423639 (2024), https://doi.org/10.1007/s10409-024-23639-x

1. Introduction

The wing is a critical part of determining the performance of aircraft. Traditional fixed wings use certain rigid deformable components to alter the wing's aerodynamic shape, which limits the adaptability and in-flight performance of aircraft [1,2]. In comparison, morphing aircraft [3] can flexibly alter wing shapes to achieve optimal aerodynamic performance under different flight states and flow field conditions, which will significantly improve their comprehensive performance [4-7]. Their emergence and development have become one of the most important trends of future aircraft.

Accurately measuring the full-field dynamic deformation of morphing aircraft wings is a critical task in aircraft research, testing, and service. The wing deformation can alter the distribution of external aerodynamic and internal structural loads [8], and even seriously affect the structure safety [9]. In addition, the measured deformation information needs to be fed back to the control and actuation systems for accurate and rapid adjustment to achieve the expected shape. The inability to measure the complicated wing shapes and deformations of morphing aircraft has restricted their practical application.

The present deformation monitoring techniques for morphing wings can be divided into contact and non-contact

*Corresponding authors. E-mail addresses: yan_liu@szu.edu.cn (Yan Liu); yuqifeng58@139.com (Qifeng Yu)
Executive Editor: Xinglong Gong

measurements. The conventional contact method can obtain strain information through strain gauges [10,11], optical fiber sensors [12-14], and intelligent interlayer sensors [15] mounted on the wing skin surface and inside structure. The displacement and shape data are calculated by integrating the directly measured strain. Nazeer et al. [16] developed a multimodal fiber optic shape sensing system, and the change in the shape of a morphing wing section was measured in terms of strain on the fibers. Meanwhile, the camber and deflection deformations of the SmartX prototype morphing wing were monitored by the multimodal sensing method inside the wind tunnel test, but there was a large error compared with the true value of the actuator input angle [17]. Recently, a stretchable sensing skin with S-shape multicore optical fiber implantation was adapted for three-dimensional (3D) shape sensing and external measurement of loads on flexible wing skins [18]. In addition, 3D shape reconstruction and deformation monitoring of flexible structures were reconstructed using multiple sensors to measure parameters such as pressure [19] and acceleration [20] in real-time. For the above contact approaches, the sensors are subjected to certain limitations, including fewer measurement points, a small measuring range, time-consuming installation, and intense modifications of the wing structure [14]. To avoid the above issues, the videogrammetric technique has been increasingly used for measuring aircraft wing deformation due to its advantages of simple equipment, non-contact, high-accuracy, real-time performance, and full-field measurement [21-24]. As German Space Center (DLR) and other research institutions (French Aerospace Laboratory, Netherlands Aerospace Centre, Airbus, etc.) have conducted a variety of wing deformation measurement tests utilizing videogrammetric techniques, including small aircrafts (Piaggio P180 and a glider PW-6U) to large transport aircrafts (A380 and A320) [25], and even the aileron deflection of aircraft wings (Fairchild Metro II) during flight [26]. Most previous studies focused on fixed-wing aircrafts.

As for morphing aircrafts, there are relatively fewer studies on wing full-field dynamic deformation measurement using videogrammetric technology. Simpson et al. [27] used photogrammetry to measure the wingtip twist and bending deformation of a variable-thickness wing as stiffness varies. Al-Isawi et al. [28] used stereo vision measurement technology to measure the shape and deflection information of the morphing wing during wind tunnel testing. Furthermore, a morphing wing prototype with polyimide thin film skin was accurately measured utilizing a 3D vision system [29]. In summary, these researches primarily focus on the deformation measurement of morphing wing prototypes with small deformation. Notably, variable-sweep wing can improve the lift and drag characteristics by altering the sweep angle, which optimizes the flight performance of aircraft at varying altitudes and speeds. It exhibits large and flexible deformation that is susceptible to the actuator settings and aerodynamic loads [30,31]. Currently, there is a lack of research on dynamic deformation measurement for the wing. Thus, it is necessary to accurately measure the sweep angle and span length of the wing under transient and steady state conditions. Meanwhile, accurately matching and tracking targets on wings during large deformation poses a challenge, affecting measurement accuracy. To address such problems, this paper aims to investigate a novel videogrammetric method for full-field dynamic deformation measurement of variable-sweep wings.

The rest of this paper is arranged as follows. In Sect. 2, the working procedure and method for dynamic deformation monitoring of variable-sweep wings are described in detail. In Sect. 3, the experiment is conducted to verify the proposed method on a variable-sweep wing, and the results are discussed. The conclusions are given in Sect. 4.

2. Theories and methods

2.1 Working procedure

The whole measurement system consists of a pair of dual-camera, a synchronized triggering device, and a high-performance workstation. Figure 1 illustrates the flowchart of the proposed method. The whole process is divided into the following phases:

(1) Preparation. The installed variable-sweep wing's surface is pasted with uncoded targets (circular and diagonal targets) as measured points. The dual-camera ought to be installed to provide the optimum viewing of wing deformation locations. Synchronously trigger the dual-camera before image acquisition. Calibrate the internal and external parameters of dual-camera using Zhang's method [32] before measurement.

(2) Image acquisition and processing. The dual-camera captures a series of image pairs during the wing morphing. Targets are detected utilizing the detection algorithm presented in Refs. [33,34]. Targets are matched between stereo image pairs utilizing the combined method of epipolar geometry constraint [35] and topological constraints. The method of affine transformation combined with adjacent closest point matching is proposed to track targets between time-series images (Sect. 2.2).

(3) Deformation calculation and analysis. With the dual-camera calibration parameters and the matched corresponding points, the 3D coordinates of measured points are calculated based on the binocular vision measurement principle (Sect. 2.3). Eventually, the wing dynamic deformation information can be obtained and analyzed by establishing deformation parameters calculation model (Sect. 2.4).

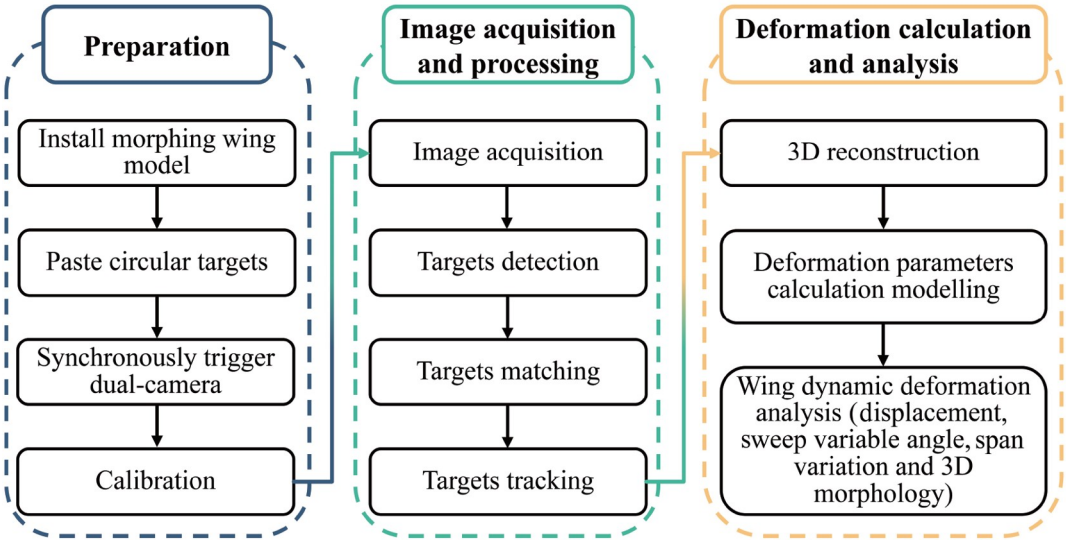

Figure 1 Full process chart of the videogrammetric method.

2.2 Targets matching and tracking

The goal of target matching and tracking is to find the corresponding targets in stereo images and time-series images, respectively. For stereo matching of the targets, a matching method is proposed that combines epipolar geometry constraint with topological constraint. The detailed procedures are as follows.

Step 1. Epipolar geometry constraint is used for matching the corresponding targets between the left and right images initially. As Fig. 2 shows, a spatial point P is imaged in the left camera C_l noted p_1 and in the right camera C_r noted p_2. If one of the image points in the left image is known (such as p_1), so another image point p_2 must be on the epipolar line l_2 corresponding to the image point p_1 on this image. The epipolar line l_2 can be calculated

$$l_2 = \mathbf{F}p_1 = \begin{bmatrix} a \\ b \\ c \end{bmatrix}, \tag{1}$$

where $\mathbf{F}$ is the fundamental matrix; a, b, and c are three components of the epipolar line l_2. As shown in Fig. 3, we search for the points near the epipolar line l_2 in the right image using the constraint condition of distance threshold λ like p_A, p_B, and p_C

$$\begin{bmatrix} u_2 & v_2 & 1 \end{bmatrix} \begin{bmatrix} a \\ b \\ c \end{bmatrix} \le \lambda, \tag{2}$$

where u_2 and v_2 are the pixel coordinates of the image points to be processed in the C_r image. λ is usually given as ±5-10 pixels [36], creating the band searching area.

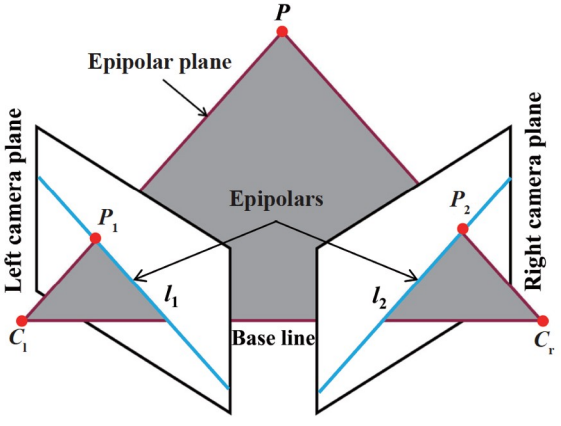

Figure 2 Epipolar geometry constraint.

Step 2. The targets in the searching area of the right image are considered as the candidate targets. Based on the topological constraint, the candidate target that has a maximum similarity of topological eigenvector with that of the point to be matched is determined as the best matching point. For any target in both left and right images, the topological eigenvector can be calculated as follows. Taking point A in the left image of Fig. 3 as an example, it is the nearest K points are searched and arranged from near to far. The distances between point A and the K points are defined as ρ_{1k} (k = 1, 2, …, K). The angles between the lines connecting point A to the K points and the u axis of the image coordinate system are defined as α_{1k} (k = 1, 2, …, K). The topological eigenvector of point A consists of ρ_{1k} and α_{1k}, i.e., $\gamma_{1A} = (\rho_{1k}, \alpha_{1k})$, ($k$ = 1, 2, …, K). Similarly, the topological eigenvectors of J candidate targets can be obtained and noted as γ_{2j} (j = 1, 2, …, J). The Euclidean distances between γ_{1A} and γ_{2j} are computed to evaluate the similarity of p_{1A} and the candidate targets. The one among the J candidate targets that has minimum Euclidean distance (maximum similarity S_{max}) is determined as the corresponding point (p_{2A}).

Step 3. Perform steps 1 to 2 repeatedly and eliminate false matches using the random sample consensus (RANSAC)

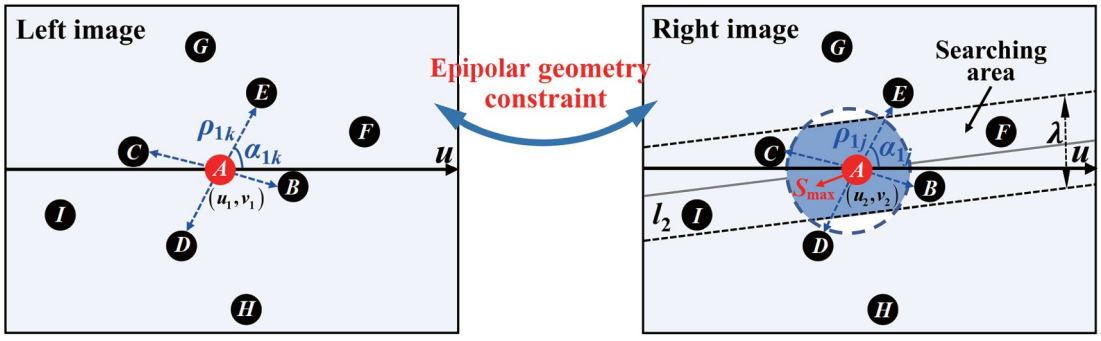

Figure 3 Establishment of the searching area and topological eigenvectors of reference point p_A.

algorithm [37], until the all of targets are correctly matched.

As for the targets tracking in time-series images with large deformation, a tracking method of affine transformation combined with adjacent closest point matching. The procedure is as follows.

Step 1. Several diagonal targets are selected as control points. They are matched in continual two images using the adjacent closest point matching and topological structure line constraint.

Step 2. The least square method is used to solve the initial values of the global affine transformation matrix for multiple control point pairs, as shown in Eq. (3)

$$\begin{bmatrix} x' \\ y' \\ 1 \end{bmatrix} = \begin{bmatrix} h_{11} & h_{12} & h_{13} \\ h_{21} & h_{22} & h_{23} \\ h_{31} & h_{32} & h_{33} \end{bmatrix} \begin{bmatrix} x \\ y \\ 1 \end{bmatrix}, \tag{3}$$

where (x, y) and (x', y') are pixel coordinates of corresponding targets in the reference and current images (see Fig. 4).

Multiplying both sides of Eq. (3) by $1/h_{33}$ to solve for x' and y'

$$\begin{cases} x' = \dfrac{h_{11}x + h_{12}y + h_{13}}{h_{31}x + h_{32}y + h_{33}}, \\ y' = \dfrac{h_{21}x + h_{22}y + h_{23}}{h_{31}x + h_{32}y + h_{33}}, \end{cases} \tag{4}$$

where the homography matrix **H** has eight unknown quantities, and is uniquely solved utilizing at least four pairs of control points (avoiding three-point collinear).

Step 3. Based on the affine transform matrix, the mapped points in the current image are obtained corresponding to the central coordinates of targets to be matched (such as p_C) in the reference image, as shown in Fig. 4. Then the adjacent closest point matching is used to determine and track the truth corresponding targets (like p_E).

Step 4. Analyze the distribution of targets, iteratively optimize the affine transformation matrix by partitioning and guide re-matching of targets based on the RANSAC algorithm.

Eventually, the target tracking in time-series images of the wing dynamic deformation can be achieved.

2.3 Binocular vision measurement principle

Based on the binocular vision measurement theory, the pinhole camera model describes the mapping relationship between a spatial object and its two-dimensional image [38]. In this study, the stereo-vision measurement system consists of a dual-camera, which is used for capturing images of the same object from different locations simultaneously. As is seen in Fig. 5, the 3D coordinate of an arbitrary spatial point is set to P (X_W, Y_W, Z_W) in the world coordinate system W-$X_WY_WZ_W$. The pixel coordinates are p_l (u_l, v_l) and p_r (u_r, v_r) in the left camera and the right camera respectively. The left and right camera coordinate systems are denoted by C_l-$X_{cl}Y_{cl}$ Z_{cl} and C_r-$X_{cr}Y_{cr}Z_{cr}$ respectively.

According to the pinhole camera model principle [38], we have

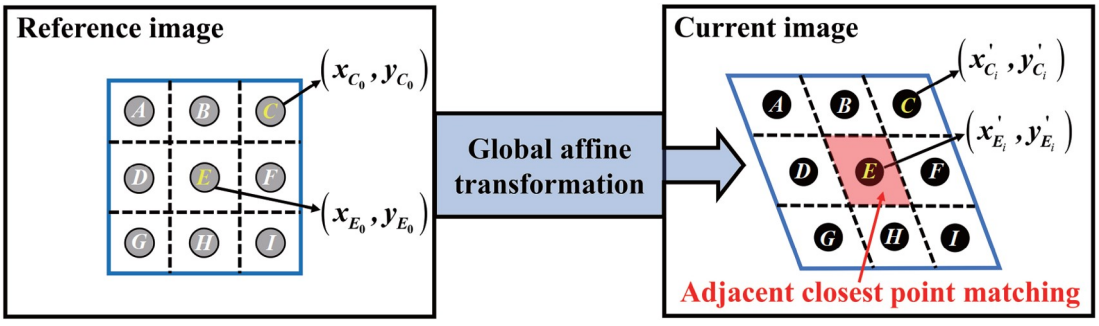

Figure 4 Tracking process of corresponding points between reference and current images.

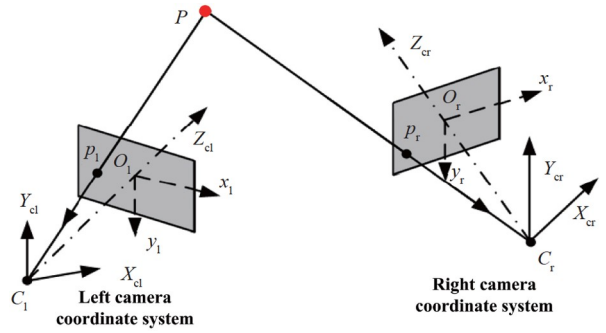

Figure 5 Geometric model of videogrammetry 3D measurement.

$$Z_{\mathrm{cl}}\begin{bmatrix} p_{\mathrm{l}} \\ 1 \end{bmatrix} = \mathbf{A}_{\mathrm{l}}\begin{bmatrix} \mathbf{R}_{\mathrm{l}} & T_{\mathrm{l}} \end{bmatrix}\begin{bmatrix} P \\ 1 \end{bmatrix},$$
$$\text{with } \mathbf{A}_{\mathrm{l}} = \begin{bmatrix} F_{x\mathrm{l}} & s_{\mathrm{l}} & u_{\mathrm{l}} \\ 0 & F_{y\mathrm{l}} & v_{\mathrm{l}} \\ 0 & 0 & 1 \end{bmatrix}, \tag{5}$$

$$Z_{\mathrm{cr}}\begin{bmatrix} p_{\mathrm{r}} \\ 1 \end{bmatrix} = \mathbf{A}_{\mathrm{r}}\begin{bmatrix} \mathbf{R}_{\mathrm{r}} & \mathbf{T}_{\mathrm{r}} \end{bmatrix}\begin{bmatrix} P \\ 1 \end{bmatrix},$$
$$\text{with } \mathbf{A}_{\mathrm{r}} = \begin{bmatrix} F_{x\mathrm{r}} & s_{\mathrm{r}} & u_{\mathrm{r}} \\ 0 & F_{y\mathrm{r}} & v_{\mathrm{r}} \\ 0 & 0 & 1 \end{bmatrix}, \tag{6}$$

where $\mathbf{A}_{\mathrm{l}}$ and $\mathbf{A}_{\mathrm{r}}$ are the intrinsic matrices of the left camera and right camera; $(F_{x\mathrm{l}}, F_{y\mathrm{l}})$ and $(F_{x\mathrm{r}}, F_{y\mathrm{r}})$ are defined as the normalized focal length of the two cameras; s is the skew, s_{l} and s_{r} are 0 [35].

The relationship between the left and right camera coordinate systems can be expressed as

$$\begin{bmatrix} X_{\mathrm{cr}} \\ Y_{\mathrm{cr}} \\ Z_{\mathrm{cr}} \end{bmatrix} = \mathbf{R}_{\mathrm{lr}}\begin{bmatrix} X_{\mathrm{cl}} \\ Y_{\mathrm{cl}} \\ Z_{\mathrm{cl}} \end{bmatrix} + \mathbf{T}_{\mathrm{lr}},$$
$$\text{with } \mathbf{R}_{\mathrm{lr}} = \begin{bmatrix} r_{11} & r_{12} & r_{13} \\ r_{21} & r_{22} & r_{23} \\ r_{31} & r_{32} & r_{33} \end{bmatrix} \text{ and } \mathbf{T}_{\mathrm{lr}} = \begin{bmatrix} T_x \\ T_y \\ T_z \end{bmatrix}, \tag{7}$$

where $\mathbf{R}_{\mathrm{lr}}$ and $\mathbf{T}_{\mathrm{lr}}$ are defined as the rotation matrix and translation vector from the left camera coordinate system to the right camera coordinate system, respectively.

For the 3D coordinates of arbitrary spatial point P_i and corresponding image projections $(p_{\mathrm{l}i}, p_{\mathrm{r}i})$ also meet the Eqs. (5)-(7). Assuming $\mathbf{M}_{\mathrm{l}} = \mathbf{A}_{\mathrm{l}}[\mathbf{R}_{\mathrm{l}}|\mathbf{T}_{\mathrm{l}}]$ and $\mathbf{M}_{\mathrm{r}} = \mathbf{A}_{\mathrm{r}}[\mathbf{R}_{\mathrm{r}}|\mathbf{T}_{\mathrm{r}}]$ represent the prospective matrixes of the left and right cameras respectively, with the known dual-camera parameters ($\mathbf{A}_{\mathrm{l}}$, $\mathbf{A}_{\mathrm{r}}$, $\mathbf{R}_{\mathrm{l}i}$, $\mathbf{T}_{\mathrm{l}i}$, $\mathbf{R}_{\mathrm{r}i}$, $\mathbf{T}_{\mathrm{r}i}$, $\mathbf{R}_{\mathrm{lr}}$, $\mathbf{T}_{\mathrm{lr}}$), so $\mathbf{X}_{wi}$ can be computed based on the least-square method as follows:

$$\mathbf{X}_{wi} = \left(\mathbf{B}^{\mathrm{T}} \cdot \mathbf{B}\right)^{-1} \cdot \mathbf{B}^{\mathrm{T}} \cdot \mathbf{C}, \tag{8}$$

where

$$\mathbf{B} = \begin{bmatrix} M_{\mathrm{l}(1,1)} - M_{\mathrm{l}(3,1)}u_{\mathrm{l}} & M_{\mathrm{l}(1,2)} - M_{\mathrm{l}(3,2)}u_{\mathrm{l}} & M_{\mathrm{l}(1,3)} - M_{\mathrm{l}(3,3)}u_{\mathrm{l}} \\ M_{\mathrm{l}(2,1)} - M_{\mathrm{l}(3,1)}v_{\mathrm{l}} & M_{\mathrm{l}(2,2)} - M_{\mathrm{l}(3,2)}v_{\mathrm{l}} & M_{\mathrm{l}(2,3)} - M_{\mathrm{l}(3,3)}v_{\mathrm{l}} \\ M_{\mathrm{r}\,(1,1)} - M_{\mathrm{r}\,(3,1)}u_{\mathrm{r}} & M_{\mathrm{r}\,(1,2)} - M_{\mathrm{r}\,(3,2)}u_{\mathrm{r}} & M_{\mathrm{r}\,(1,3)} - M_{\mathrm{r}\,(3,3)}u_{\mathrm{r}} \\ M_{\mathrm{r}\,(2,1)} - M_{\mathrm{r}\,(3,1)}v_{\mathrm{r}} & M_{\mathrm{r}\,(2,2)} - M_{\mathrm{r}\,(3,2)}v_{\mathrm{r}} & M_{\mathrm{r}\,(2,3)} - M_{\mathrm{r}\,(3,3)}v_{\mathrm{r}} \end{bmatrix}, \mathbf{C} = \begin{bmatrix} u_{\mathrm{l}}M_{\mathrm{l}(3,4)} - M_{\mathrm{l}(1,4)} \\ v_{\mathrm{l}}M_{\mathrm{l}(3,4)} - M_{\mathrm{l}(2,4)} \\ u_{\mathrm{r}}M_{\mathrm{r}(3,4)} - M_{\mathrm{r}(1,4)} \\ v_{\mathrm{r}}M_{\mathrm{r}(3,4)} - M_{\mathrm{r}(2,4)} \end{bmatrix}.$$

2.4 Dynamic deformation parameters calculation modelling

To obtain full-field dynamic deformation information of the variable-sweep wing, the calculation and analysis model is established, as shown in Fig. 6. The airframe coordinate system O-$X_AY_AZ_A$ is defined as the world coordinate system (see Fig. 6a). The X_A axis goes in the airflow direction, the Y_A axis is in the spanwise direction, the Z_A axis is perpendicular to the wing surface upwards, and the target located at the wing root position is select as the origin O. With the obtained rotation matrix and translation vector between the left and right camera coordinate system using Zhang's method [32], the 3D coordinates $\mathbf{X}_{C_1}$ of all targets in the left camera coordinate system are calculated. They need to be uniformly converted to the airframe coordinate system using the following equations:

$$\mathbf{X}_A = \mathbf{R}_{C_1A}\mathbf{X}_{C_1} + \mathbf{T}_{C_1A}, \tag{9}$$

where $\mathbf{X}_A$ are the 3D coordinates of targets in the airframe coordinate system; $\mathbf{R}_{C_1A}$ and $\mathbf{T}_{C_1A}$ represent the rotation matrix and translation vector from the left camera coordinate system to the airframe coordinate system. They are derived as

$$\begin{cases} \mathbf{R}_{C_1A} = \left(\mathbf{R}_{AC_1}\right)^{-1}, \\ \mathbf{T}_{C_1A} = -\mathbf{R}_{C_1A}\mathbf{T}_{AC_1}, \end{cases} \tag{10}$$

where $\mathbf{T}_{C_1A}$ is the 3D coordinate of the origin of the airframe coordinate system in the left camera coordinate system; $\mathbf{R}_{C_1A}$ can be computed as follows:

$$\mathbf{R}_{AC_1} = \begin{bmatrix} \mathbf{n}_{X_A} & \mathbf{n}_{Y_A} & \mathbf{n}_{Z_A} \end{bmatrix}, \tag{11}$$

where $\mathbf{n}_{X_A}$, $\mathbf{n}_{Y_A}$, and $\mathbf{n}_{Z_A}$ are the unit vectors of the three coordinate axes of the airframe coordinate system in the left camera coordinate system.

As shown in Fig. 6b, the 3D coordinates of targets in the

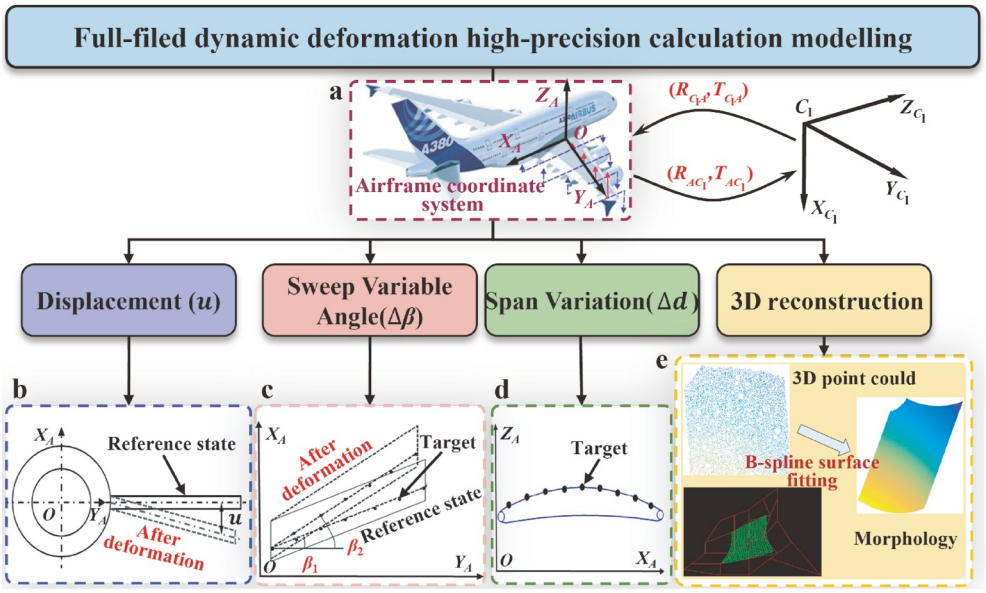

Figure 6 Full-field dynamic deformation high-accuracy calculation and analysis model: **a** airframe coordinate system; **b** displacement; **c** sweep variable angle; **d** span variation; **e** 3D reconstruction.

airframe coordinate system are denoted as X_{A0} (X_{A0}, Y_{A0}, Z_{A0}) at the initial reference state. After deformation, the displacement of targets can be computed as

$$\begin{cases} u_{X_A} = X_{Ai} - X_{A0}, \\ u_{Y_A} = Y_{Ai} - Y_{A0}, \\ u_{Z_A} = Z_{Ai} - Z_{A0}, \end{cases} \tag{12}$$

where X_{Ai}, Y_{Ai}, and Z_{Ai} are the 3D coordinates of targets on the wing after deformation.

In this research, the sweep variable angle is defined as the changing value of the leading edge sweep angle β, and it is the positive value when the wing is cambered ahead. As illustrated in Fig. 6c, in the X_AY_A plane of the airframe coordinate system, the solid and dashed lines represent the wing before and after deformation, respectively. The line equation for a row of targets along the span direction near the leading edge of the wing in the X_AY_A plane is fitted using the least squares method as follows:

$$mX_A + nY_A + c = 0, \tag{13}$$

where m, n, and c are the parameters of this fitted line.

The leading edge sweep angle β can be derived as

$$\cos\beta = |\mathrm{n}| / \sqrt{m^2 + n^2}. \tag{14}$$

Assume that β_1 and β_2 are denoted as the leading edge sweep angle with the wing before and after deformation, respectively. The leading edge sweep variable angle $\Delta\beta$ is equal to $\beta_2 - \beta_1$.

As for the span variation during wing morphing, the targets on the wing root profile are obtained using spatial plane fitting based on the following equation:

$$AX_A + BY_A + CZ_A + D = 0, \tag{15}$$

where A, B, C, and D are parameters of the space plane.

We define d as the distance from the airframe coordinate system origin O to the spatial plane in which the wing profile is located (see Fig. 6d). The span variation Δd is the difference between the distances d_1 and d_2 of the wing before and after deformation

$$\Delta d = d_1 - d_2 = \frac{|D_1|}{\sqrt{A_1^2 + B_1^2 + C_1^2}} - \frac{|D_2|}{\sqrt{A_2^2 + B_2^2 + C_2^2}}, \tag{16}$$

where (A_1, B_1, C_1, D_1) and (A_2, B_2, C_2, D_2) are plane equation parameters of the wing tip profile before and after deformation.

As illustrated in Fig. 6e, to reconstruct the configuration of the wing surface, the 3D coordinates $\mathbf{X}_{Ai}$ of all targets under the airframe coordinate system are linearly interpolated. Then, the interpolated point clouds $\mathbf{Q}_i$ are fitted using B-sample surface fitting [39], as shown in Eq. (17)

$$\begin{aligned} &S(u,v) = \left[\mathbf{N}_{k,p}(u)\right]^{\mathrm{T}} \left[\mathbf{Q}_{k,l}\right] \left[\mathbf{N}_{l,q}(v)\right], \\ &m - p \le k \le m,\ n - q \le l \le n, \end{aligned} \tag{17}$$

where $\mathbf{Q}_{k,l}$ are the control point matrixes of $(p+1) \times (q+1)$; $[\mathbf{N}_{k,p}(u)]^{\mathrm{T}}$ and $[\mathbf{N}_{l,q}(v)]$ are column vectors of $1 \times (p+1)$ and $(q+1) \times 1$ respectively.

3. Experimental verification and results analysis

To verify the accuracy of the proposed method for wings with large deformation, a dynamic deformation measurement experiment based on a variable-sweep wing model was performed.

3.1 Experimental setup

The experimental setup is illustrated in Fig. 7a. The equipment mainly included a dual-camera, a synchronized triggering device, a host computer, and a scale bar. There were 163 circular targets and 15 diagonal targets adhered to the wing surface. A dual-camera consisted of two HKROBOT MV-CH089-10UM industrial cameras with image resolutions of 4096 × 2160 pixels. The pixel size is 3.45 μm × 3.45 μm, and the maximum frame rate is 32 fps. The type of camera lens is Computar-MPW2 with small distortion, its focal length is 12 mm, and the aperture factor ranges from F2.4 to F16. The cameras and lenses were adjusted to ensure that targets on the entire wing surface could be viewed with clear imaging. In order to prevent motion blurring during wing morphing, we set the exposure time of the camera as short as possible. The synchronized triggering device can generate two-channel signals, which trigger the dual-camera to capture images asynchronously. The acquired images were collected and stored in the host computer through Ethernet cables. The BRUNSON scale bar was used to validate the measurement precision of the system. The geometric size of the variable-sweep wing model is 535 mm × 470 mm. The sequential images were captured by the dual-camera during the dynamic morphing of the wing through the actuator. Figure 7b and c were the original left and right images of the maximum morphing wing.

3.2 Calibration results

Before measurement, the dual-camera was triggered to capture 28 pairs of images of a checkerboard calibration board (400 mm × 300 mm) at its different positions and orientations.

The calibration board was placed as close to the wing plane as possible, which ensured it remained within the dual-camera's depth of field. Zhang's calibration method [32] was employed to acquire the intrinsic, extrinsic, and distortion parameters of the dual-camera, as shown in Table 1. The rotation matrix and translation vector describe the relative relationship between the left and right camera coordinate systems.

3.3 Detection and matching of targets

The acquired image pairs of the variable-sweep wing are processed by the proposed targets detection method, which exhibits sub-pixel positioning and higher extraction efficiency. The detected results of the targets on the wing surface are shown in Fig. 8a and b. The centers of targets are

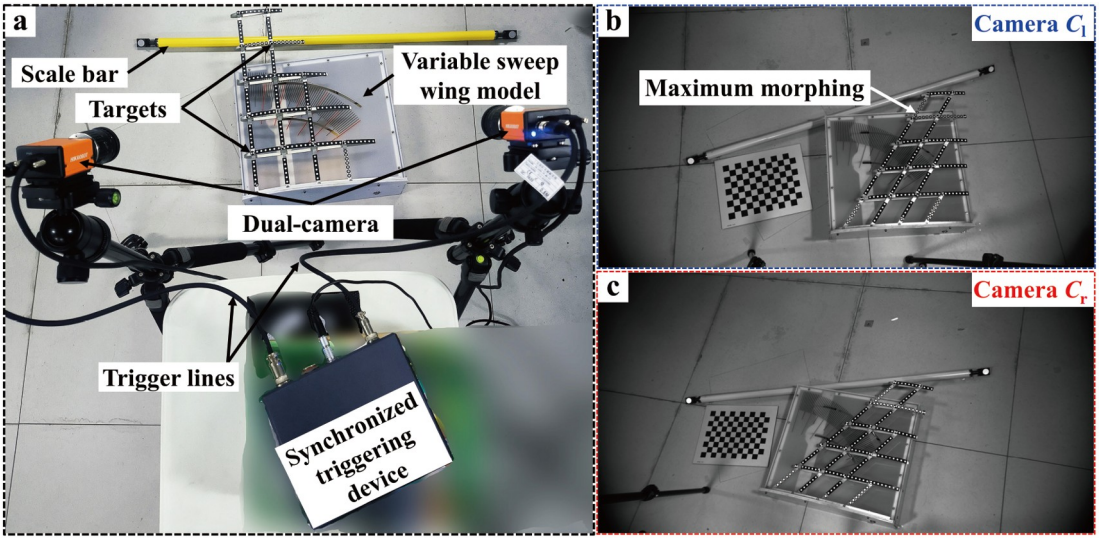

Figure 7 **a** Experimental setup of the wing dynamic deformation measurement; **b** and **c** are original images of the maximum morphing wing captured by the dual-camera.

Table 1 The intrinsic and extrinsic parameters of the dual-camera calibratio

The intrinsic parameters of dual-camera	Left camera	Right camera
Focal length	[34941456, 34946600]	[35002305, 35018304]
Principal point	[20740113, 10922497]	[20673412, 10999634]
Radial distortion	[−0.0447, 0.3045]	[−0.0486, 0.3001]
The extrinsic parameters of dual-camera	$\mathbf{R}_{lr} = \begin{bmatrix} 0.9265 & -0.2146 & 0.3093 \\ 0.2069 & 0.9767 & 0.0580 \\ -0.3145 & 0.0102 & 0.9492 \end{bmatrix}$, $\mathbf{T}_{lr} = \begin{bmatrix} -547.5356 \\ -64.6570 \\ 137.0308 \end{bmatrix}$	

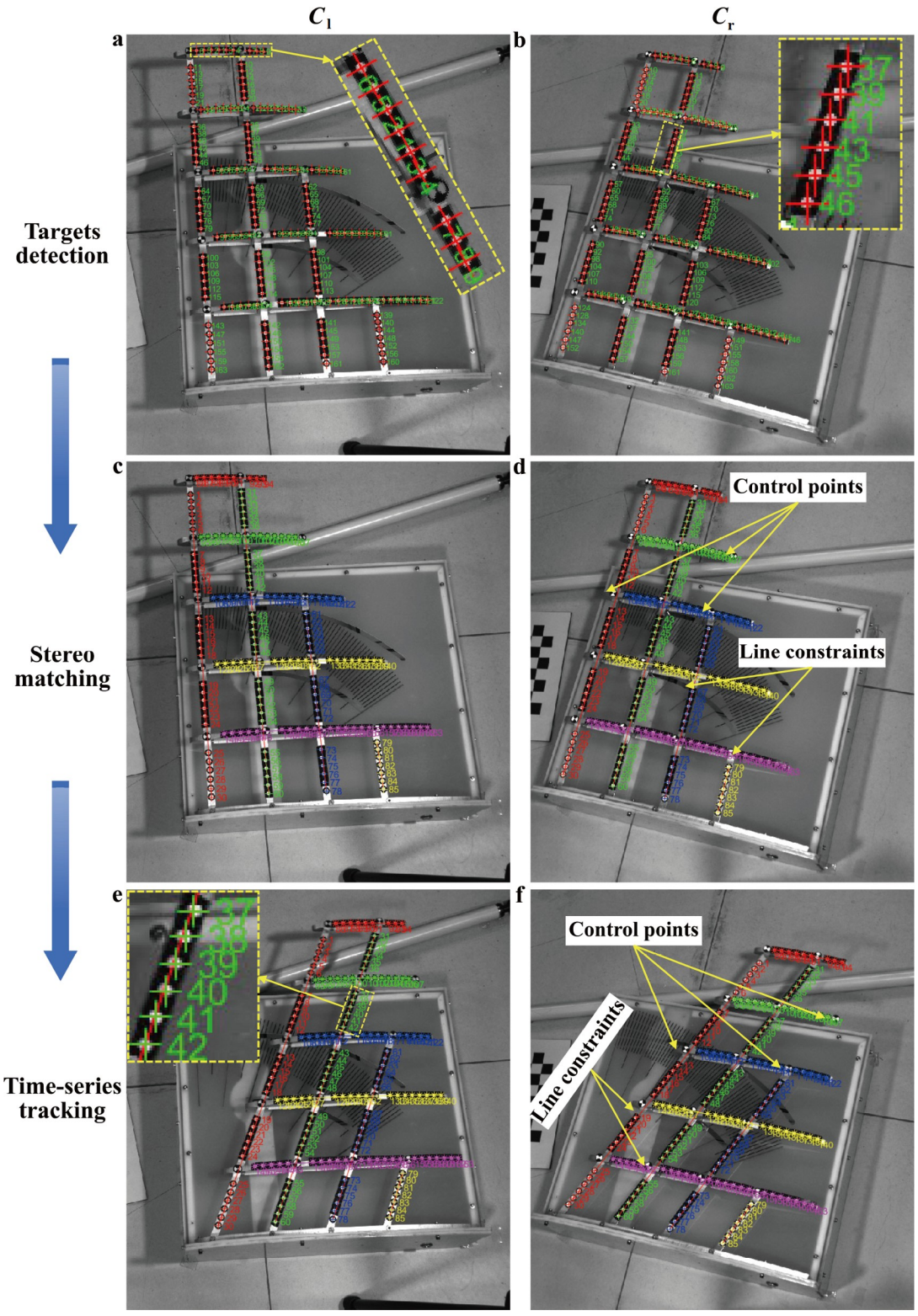

Figure 8 **a** and **b** are detected results of the targets center; **c** and **d** are stereo matching results of targets in the reference state; **e** and **f** are time-series tracking results of targets in the current state.

marked as red "+" and their IDs are denoted as the numbers in green. Thus, the detection algorithm for circular targets.

Using the matching method described in Sect. 2.2, the matched results of the targets between stereo image pairs are shown in Fig. 8c and d. For the targets viewed in both of left and right cameras, there is no false match case. The complexity of corresponding target matching is decreased. Hence, the proposed matching method based on the epipolar

geometry constraint and topological constraint is rapid and accurate.

The tracked results of the targets in time-series images are obtained using the presented method. Firstly, the diagonal targets used as control points are matched in the reference and current deformed images based on line constrain. Then the circular targets are matched using the proposed tracking method of affine transformation combined with adjacent closest point matching. The RANSAC algorithm is performed to iteratively optimize the affine transformation matrix and guide the re-matching of targets. As can be seen in Fig. 8c and e (or d and f), all targets are correctly tracked under the occurrence of large deformation in the wing.

3.4 Accuracy verification

According to the VDI_2634 optical test standard [40], a high-accuracy scale bar is employed to verify the measurement precision of the presented method and system. As is seen in Fig. 7a, the length between its two circular targets of a BRUNSON scale bar is 1100 mm with the uncertainty of ± 1.5 μm. Figure 9 shows the length measurement result of the scale bar compared with the real value of 1100 mm. The length error is denoted as the difference between the measured and the known real value, and the maximum is less than 0.32 mm. The actual accuracy of the proposed method is approximately 0.02% of the observed area (e.g., 0.32 mm on a 1.6 m scale), which confirms the validity of the measurement system.

3.5 Measurement of sweep variable angle and span variation

With the obtained 3D coordinates of targets in the airframe coordinate system, the sweep variable angle and span variation of the morphing wing can be calculated using the established calculation model, as illustrated in Fig. 10. It is found that the sweep variable angle increased from the initial 0° (stage I) to the maximum of 36.6° (stage II), and then gradually decreased to the initial position during the morphing process (stage III). Meanwhile, the span variation has a similar trend, and the maximum value is 101.13 mm (stage II). The above results are consistent with the deformation law of the variable-sweep wing revolving around its root. Therefore, the presented method can effectively measure the key dynamic deformation parameters of a morphing wing aircraft in the course of changing the angle of sweep.

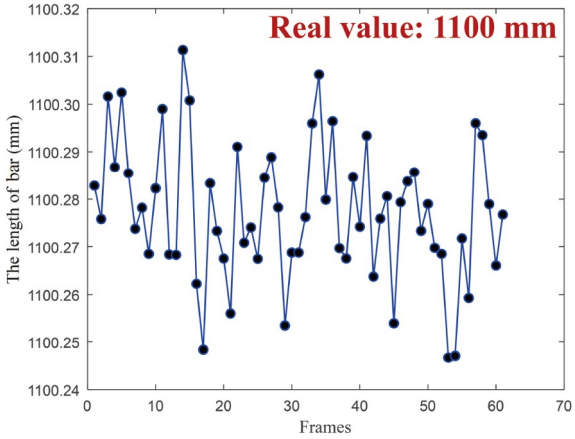

Figure 9 Validation results for length measurement accuracy of the scale bar.

3.6 Displacement measurement

The displacement of all targets on the wing surface is calculated by subtracting the 3D coordinates before and after deformation. The displacement of all targets increases gradually, and then decreases in the wing morphing course. Figure 11 indicates the displacement of targets distributed in the spanwise direction. It is found that the displacement of any wing beam increases as it gets farther from the wing root. In addition, there is a sawtooth segment rise in the displacement-increasing phase. The most probable reason is that gear positive transmission in the actuator with the morphing wing prototype is not stable.

Figure 12 depicts the displacement of targets distributed along the chord direction. It is found that the displacement of the targets on the same wing rib is very consistent. In the deformed state of maximum sweep angle, the displacement of the farthest wing rib (the red rectangle) from the wing root reaches the maximum of 322.72 mm (Fig. 12b), and the displacement of the closest wing rib (the pink rectangle) is 64.86 mm (Fig. 12d). The results are conformed to the practical deformation law overall.

3.7 3D reconstruction of the wing dynamic morphing

The 3D shape reconstruction of the wing under different morphing states is performed. The 3D coordinates of targets in the airframe coordinate system are plotted in the X_AY_A plane as shown in Fig. 13. It depicts the structural change of the wing from the initial stationary state to the deformed state of maximum sweep angle.

The interpolation and curve fitting functions in Sect. 2.4 are used for reconstructing the 3D surface from the 3D coordinates of the targets on the wing surface. Figure 14 shows the reconstructed 3D full-field shapes of the variable-sweep wing in a dynamic morphing process. It can be observed that the surface shapes have features of good smoothing and bending. The wing leading edge root position is slightly higher, whereas the trailing edge portion is relatively lower. Combining Figs. 13 and 14, this variable-sweep wing is morphed in the X_AY_A plane, which belongs to

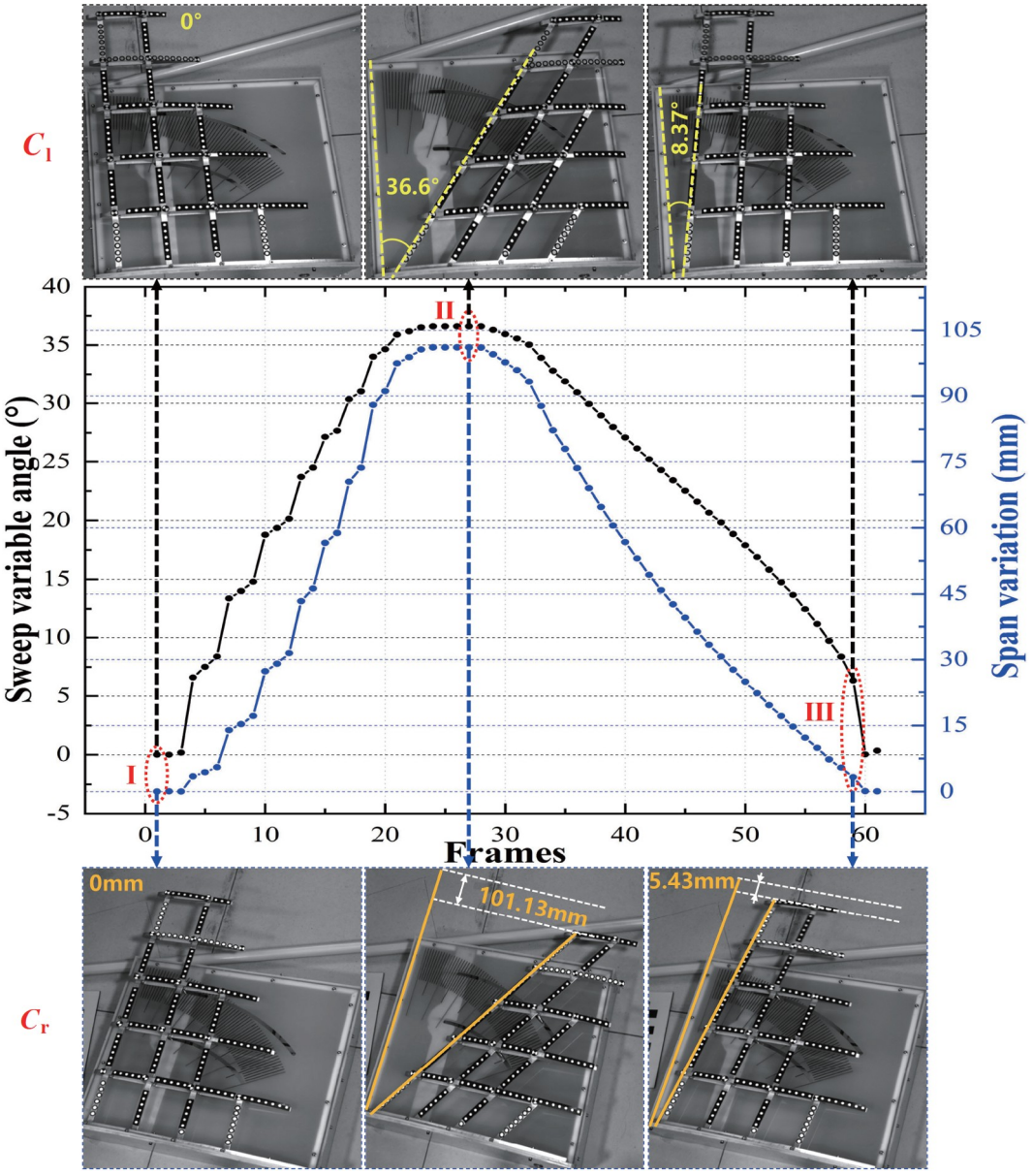

Figure 10 Calculation results and variations of dynamic morphing control parameters for the wing.

the in-plane morphing wing. The results indicate that the overall configuration of the wing surface can be effectively reconstructed and dynamically displayed under different morphing states. The obtained full-field deformation information can be used to realize real-time feedback of the current morphing geometry and dynamic deformation monitoring, which enable the closed-loop control and safety evaluation of morphing wings.

4. Conclusions

In this paper, a novel videogrammetric method is proposed to monitor full-field dynamic deformation of variable-sweep wings with active large deformation. Present matching and tracking methods for corresponding targets between sequential image pairs. Based on the principle of binocular vision measurement, the 3D coordinates of targets on the wing are calculated. The full-field dynamic deformation calculation model is established for calculating various deformation parameters. The validity and accuracy of the presented method are verified by experiments performed on a variable-sweep wing model. The results indicate that the actual accuracy of the proposed method is approximately 0.02% of the measured area (e.g., 0.32 mm in a 1.6 m scale). The full-field dynamic deformation of the wing is measured accurately. The measurement results conform to the actual deformation law of the variable-sweep wing revolving around its root. This research may not only benefit the closed-loop control of morphing wings, but also provide

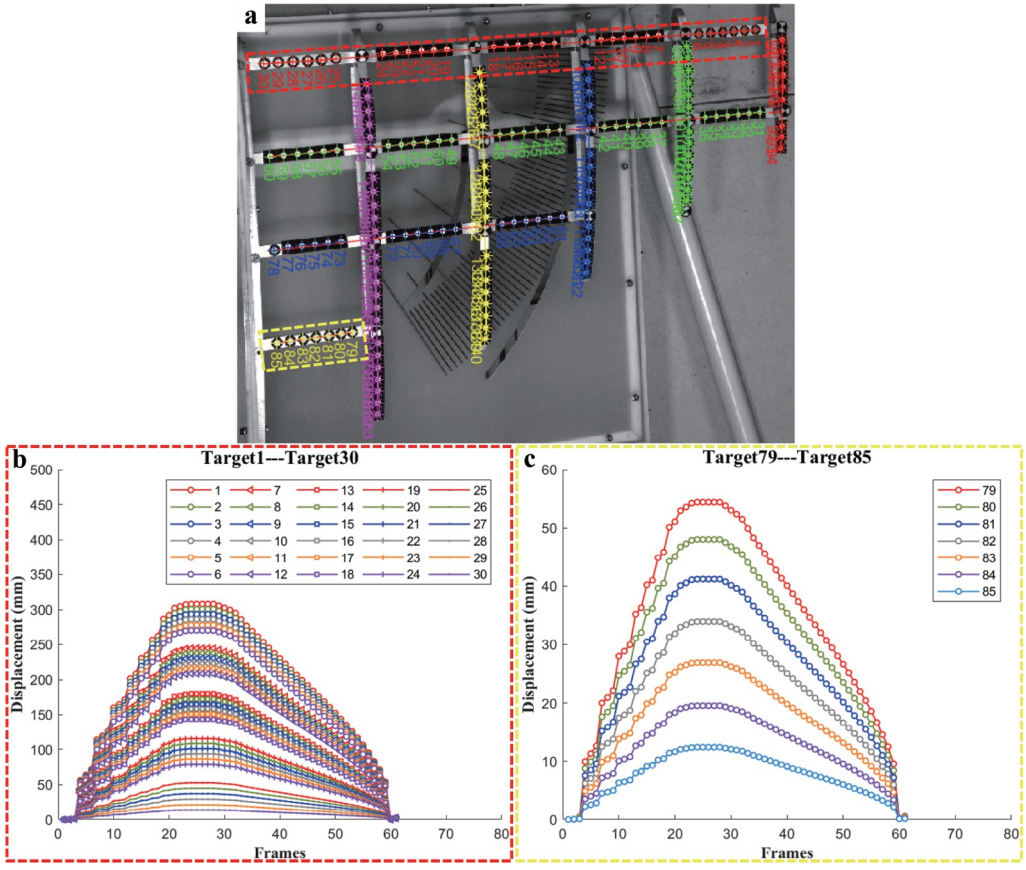

Figure 11 Displacement of targets distributed along the spanwise direction.

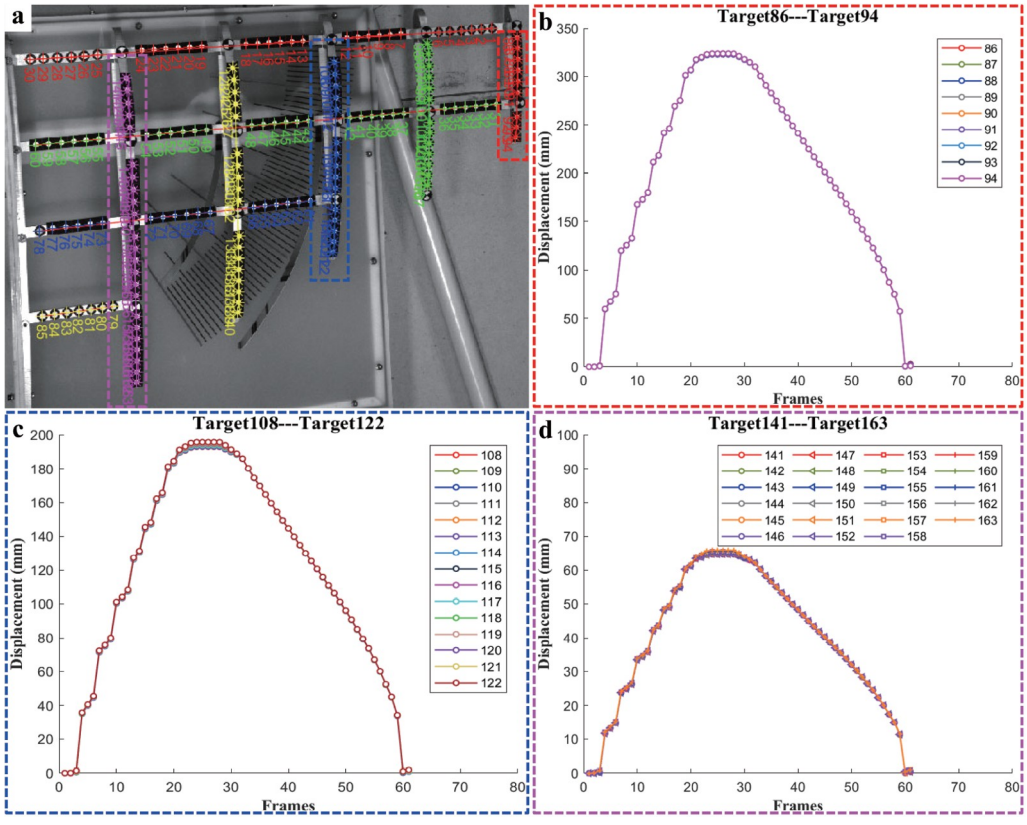

Figure 12 Displacement of targets distributed along the chord direction.

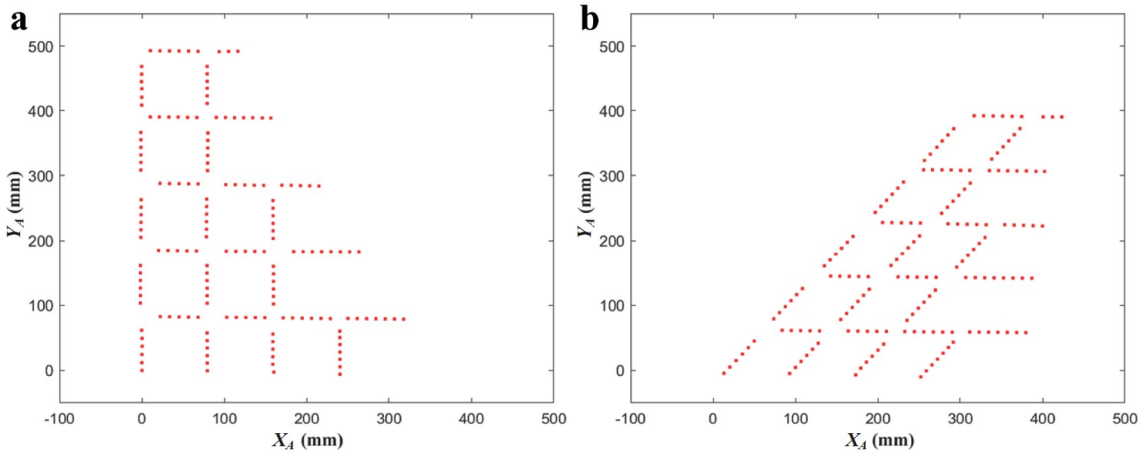

Figure 13 Dynamic morphing process of the wing in the X_AY_A plane.

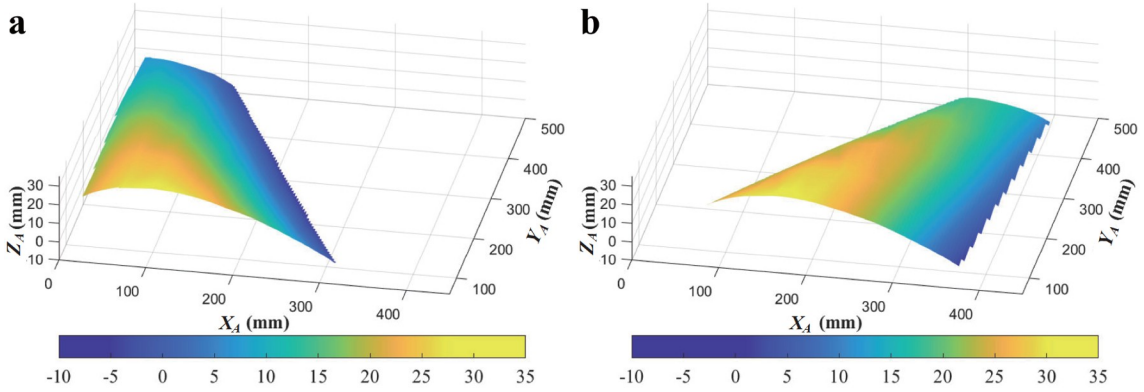

Figure 14 Reconstructed 3D full-field shapes of the wing in a dynamic morphing process.

deformation information to check the aerodynamic characteristics and assist in the safety evaluation of wing structures.

Conflict of interest *On behalf of all authors, the corresponding author states that there is no conflict of interest.*

Author contributions *Liqiang Gao designed the research, performed the experiments, processed the experiment data, and wrote the original draft of the manuscript. Yan Liu acquired financial support, designed the research, and revised the manuscript. Bin Jiang and Zhendong Ge set up the experimental device. Haoyang Li performed the experiments. Xiang Guo helped organize the manuscript. Tao Suo reviewed the manuscript. Qifeng Yu secured financial support, provided experimental resources, and reviewed the final version.*

Acknowledgements *This work was supported by the National Natural Science Foundation of China (Grant No. 12202282).*

1 B. Jenett, S. Calisch, D. Cellucci, N. Cramer, N. Gershenfeld, S. Swei, and K. C. Cheung, Digital morphing wing: Active wing shaping concept using composite lattice-based cellular structures, Soft Robot. **4**, 33 (2017).
2 M. Di Luca, S. Mintchev, G. Heitz, F. Noca, and D. Floreano, Bioinspired morphing wings for extended flight envelope and roll control of small drones, Interface Focus **7**, 20160092 (2017).
3 S. Barbarino, O. Bilgen, R. M. Ajaj, M. I. Friswell, and D. J. Inman, A review of morphing aircraft, J. Intel. Mat. Syst. Struct. **22**, 823 (2011).
4 L. Chu, Q. Li, F. Gu, X. Du, Y. He, and Y. Deng, Design, modeling, and control of morphing aircraft: A review, Chinese J. Aeronaut. **35**, 220 (2022).
5 J. Zhu, J. Yang, W. Zhang, X. Gu, and H. Zhou, Design and applications of morphing aircraft and their structures, Front. Mech. Eng. **18**, 34 (2023).
6 J. B. Bai, T. W. Liu, G. H. Yang, C. C. Xie, and S. Mao, A variable camber wing concept based on corrugated flexible composite skin, Aerospace Sci. Tech. **138**, 108318 (2023).
7 H. Yang, S. Jiang, Y. Wang, and H. Xiao, Design, kinematic and fluid-structure interaction analysis of a morphing wing, Aerosp. Sci. Tech. **143**, 108721 (2023).
8 T. S. S. Versiani, F. J. Silvestre, A. B. Guimarães Neto, D. A. Rade, R. G. Annes da Silva, M. V. Donadon, R. M. Bertolin, and G. C. Silva, Gust load alleviation in a flexible smart idealized wing, Aerosp. Sci. Tech. **86**, 762 (2019).
9 T. E. Noll, J. M. Brown, M. E. Perez-Davis, S. D. Ishmael, G. C. Tiffany, and M. Gaier, Investigation of the Helios Prototype Aircraft Mishap Volume I Mishap Report (NASA Langley Research Center, Hampton, 2004).
10 G. W. Reich, and B. P. Sanders, in Structural shape sensing for morphing aircraft: Proceedings of Smart Structures and Materials 2003 on Smart Structures and Integrated Systems, San Diego, 2003.
11 W. Akl, S. Poh, and A. Baz, Wireless and distributed sensing of the shape of morphing structures, Sensor. Actuat. A-Phys. **140**, 94 (2007).
12 T. L. T. Lun, K. Wang, J. D. L. Ho, K. H. Lee, K. Y. Sze, and K. W. Kwok, Real-time surface shape sensing for soft and flexible

structures using fiber bragg gratings, IEEE Robot. Autom. Lett. **4**, 1454 (2019).
13 I. Floris, J. M. Adam, P. A. Calderón, and S. Sales, Fiber optic shape sensors: A comprehensive review, Optics Lasers Eng. **139**, 106508 (2021).
14 L. Zhu, G. Sun, W. Bao, Z. You, F. Meng, and M. Dong, Structural deformation monitoring of flight vehicles based on optical fiber sensing technology: A review and future perspectives, Engineering **16**, 39 (2022).
15 Y. Kostogorova-Beller, J. Whitford, K. Dudley, A. Menon, A. Chakravarthy, and J. Steck, A study on smart SansEC skin sensing for real-time monitoring of flexible structures, IEEE Sens. J. **18**, 2836 (2018).
16 N. Nazeer, R. M. Groves, and R. Benedictus, Assessment of the measurement performance of the multimodal fibre optic shape sensing configuration for a morphing wing section, Sensors **22**, 2210 (2022).
17 N. Nazeer, X. Wang, and R. M. Groves, Sensing, actuation, and control of the SmartX prototype morphing wing in the wind tunnel, Actuators **10**, 107 (2021).
18 G. Sun, Y. Hu, Y. He, Y. Song, M. Dong, and L. Zhu, Stretchable sensing skin with S-shape multicore optical fiber implantation for morphing flight vehicles, Optik **199**, 163088 (2019).
19 X. Pu, M. Liu, X. Chen, J. Sun, C. Du, Y. Zhang, J. Zhai, W. Hu, and Z. L. Wang, Ultrastretchable, transparent triboelectric nanogenerator as electronic skin for biomechanical energy harvesting and tactile sensing, Sci. Adv. **3**, e1700015 (2017).
20 A. Hermanis, R. Cacurs, and M. Greitans, Acceleration and magnetic sensor network for shape sensing, IEEE Sens. J. **16**, 1271 (2016).
21 Q. Yu, Z. Qiu, X. Sun, and H. Lu, Three dimensional movement measurement for the wing of a flying airplane, Acta Mech. Sin. **19**, 575 (2003).
22 T. Liu, A. W. Burner, T. W. Jones, and D. A. Barrows, Photogrammetric techniques for aerospace applications, Prog. Aerosp. Sci. **54**, 1 (2012).
23 Y. Fu, Y. Shang, W. Hu, B. Li, and Q. Yu, Non-contact optical dynamic measurements at different ranges: A review, Acta Mech. Sin. **37**, 537 (2021).
24 X. Wu, and Z. Xu, Deflection monitoring of morphing winglet by binocular vision system with environment adaptability, Mech. Syst. Signal Process. **185**, 109696 (2023).
25 F. Boden, N. Lawson, H. W. Jentink, and J. Kompenhans, Advanced in-Flight Measurement Techniques (Springer Berlin, Heidelberg, 2013).
26 P. Trisiripisal, M. Parks, L. Abbott, T. Liu, and G. Fleming, in Stereo analysis for vision-based guidance and control of aircraft landing: Proceedings of the 44th AIAA Aerospace Sciences Meeting and Exhibit, Reno, 2006.
27 A. Simpson, J. Rowe, S. Smith, and J. Jacob, in Aeroelastic deformation and buckling of inflatable wings under dynamic loads: Proceedings of the 48th AIAA/ASME/ASCE/AHS/ASC Structures, Structural Dynamics, and Materials Conference, Hawaii, 2007.
28 M. M. A. Al-Isawi, and J. Z. Sasiadek, Control of flexible wing UAV using stereo camera, in: Aerospace Robotics III (Springer, Cham, 2019), pp. 97-120.
29 G. Sun, H. Li, M. Dong, X. Lou, and L. Zhu, RETRACTED: Optical fiber shape sensing of polyimide skin for a flexible morphing wing, Appl. Opt. **56**, 9325 (2017).
30 R. Kress, in Variable sweep wing design: Proceedings of Aircraft Prototype and Technology Demonstrator Symposium, Dayton, 1983.
31 L. Zeng, L. Liu, X. Shao, and J. Li, Mechanism analysis of hysteretic aerodynamic characteristics on variable-sweep wings, Chin. J. Aeronaut. **36**, 212 (2023).
32 Z. Zhang, A flexible new technique for camera calibration, IEEE Trans. Pattern Anal. Machine Intell. **22**, 1330 (2000).
33 Y. Liu, X. Su, X. Guo, T. Suo, and Q. Yu, A novel concentric circular coded target, and its positioning and identifying method for vision measurement under challenging conditions, Sensors **21**, 855 (2021).
34 C. Harris, and M. Stephens, in A combined corner and edge detector: Proceedings of Alvey vision conference, Manchester, 1988.
35 R. Hartley, Multiple View Geometry in Computer Vision (Cambridge University Press, New York, 2003).
36 M. Ye, J. Liang, L. Li, B. Qian, M. Ren, M. Zhang, W. Lu, and Y. Zong, Full-field motion and deformation measurement of high speed rotation based on temporal phase-locking and 3D-DIC, Opt. Laser. Eng. **146**, 106697 (2021).
37 M. A. Fischler, and R. C. Bolles, Random sample consensus, Commun. ACM **24**, 381 (1981).
38 P. D. Lin, and C. K. Sung, Comparing two new camera calibration methods with traditional pinhole calibrations, Opt. Express **15**, 3012 (2007).
39 Y. Kineri, M. Wang, H. Lin, and T. Maekawa, B-spline surface fitting by iterative geometric interpolation/approximation algorithms, Comput. Aided Design **44**, 697 (2012).
40 Verein Deutscher Ingenieure: VDI/VDE 2634-1, Optical 3D measuring systems: Imaging systems with point-by-point probing.

基于摄像测量的变后掠翼全场动态变形监测新方法

高利强, 刘燕, 江斌, 葛振东, 李昊阳, 郭翔, 索涛, 于起峰

摘要 变体飞行器机翼动态变形监测是实现闭环控制和评估结构安全性的关键. 针对具有主动大变形能力的变后掠机翼, 本文提出了一种机翼全场三维动态变形摄像测量方法. 首先为匹配立体图像对应的同名特征点, 提出了一种基于极线约束结合拓扑约束的立体匹配方法; 其次提出了一种基于仿射变换与邻近点匹配相结合的方法实现了大变形时序图像中特征点的快速自动跟踪; 最后建立动态变形参数分析计算模型获得了位移、后掠变角和展长变化量. 通过开展变后掠翼模型动态变形测量实验验证了所提方法的有效性. 结果表明, 所提方法的实际精度约为测量区域的0.02% (例如, 1.6 m尺度下为0.32 mm). 在一个变体历程中, 机翼后掠变角、展长变化量和位移均先增后减, 后掠变角最大为36.6°, 展长变化量达到101.13 mm, 有效重建了机翼不同变体时的整体构型.